Effect of Cd dopant on structural, optical and CO_2 gas sensing properties of ZnO thin film sensors fabricated by chemical bath deposition method

Büşra Altun[1] · Irmak Karaduman Er[2] · Ali Orkun Çağırtekin[3] · Ahmad Ajjaq[3] · Fatma Sarf[4] · Selim Acar[3]

Abstract

Cadmium-doped zinc oxide (Cd-doped ZnO) films were produced by economic facile chemical bath deposition method. The Cd doping content was adjusted as 1%, 3%, 5% and 7%. The structural, morphological and optical properties of the films were characterized by XRD, Raman, SEM and UV–Vis. The response in a carbon dioxide atmosphere was measured by varying the concentration up to 100 ppm at different working temperatures (30–250 °C). XRD measurements demonstrated that all synthesized films have a good crystallite structure with hexagonal wurtzite dominant phase. A large variety of nanostructures are randomly distributed over the films' surfaces depending on Cd doping content as was manifested by the corresponding SEM images. From the transmittance analysis, an ultraviolet absorption edge corresponding to pure ZnO film undergoes a redshift with the increase in Cd content. The results from Raman spectra are in good agreement with the XRD results. From the gas sensing measurements, a high response toward 100 ppm CO_2 gas was detected by 3% Cd-doped ZnO sensor (88.24% at 125 °C) with an acceptable response of 8.36% at room temperature, which exhibited the lowest response/recovery times as well as highest selectivity, stability and reproducibility. Changes in the CO_2 gas sensing response as a function of Cd doping content are explained based on particle size, optical bandgap and surface images.

Keywords Gas sensor · Cd-doped ZnO · Chemical bath deposition · CO_2

1 Introduction

Nowadays, fossil fuel is an indispensable part in almost all industrial applications. The consumption of fossil fuels leads to high emission of carbon dioxide (CO_2) which is one of the main greenhouse gases. The rise in CO_2 emission has been recognized as the main reason of the serious environmental

danger of global warming [1]. In addition, the increasing demand for safe and quality food has led to the development of innovative approaches in food packaging and the emergence of smart packaging technology [2, 3]. CO_2 protective gas packaging is used in many foods, especially meat, milk and bakery products. If a suitable combination of CO_2 and O_2 gases is prepared, the shelf life of fresh products can be extended. However, excessive CO_2 levels are the main indicator of food spoilage in packaged foods [4]. For the reasons mentioned above, it is very important to detect the presence of CO_2 gas and control its concentration. The detection of CO_2 has been carried out utilizing different types of sensors such as catalytic, electrochemical, infrared and semiconductor [5]. Although much progress has been made in the development of CO_2 gas monitoring sensors, many of these sensors are not particularly suitable. The study of different combinations of structures (like ZnO, SnO_2, CuO, V_2O_5 and WO_3) known to improve gas sensing properties has gained importance and has been the focus of attention of researchers [6–10].

✉ Irmak Karaduman Er
irmakkaradumaner@karatekin.edu.tr

[1] Department of Advanced Technology, Graduate School of Natural and Applied Sciences, Gazi University, Ankara, Turkey

[2] Department of Medical Services and Techniques, Eldivan Medical Services Vocational School, Çankırı Karatekin University, Çankırı, Turkey

[3] Department of Physics, Faculty of Science, Gazi University, Ankara, Turkey

[4] Department of Management and Organization, Çan Vocational School, Çanakkale Onsekiz Mart University, Çanakkale, Turkey

Non-toxicity, good electrical, optical and piezoelectric properties, stability and the abundance in nature make ZnO a cheaper substance compared to today's transparent conductive oxide materials (ITO, SnO_2). ZnO is generally used as a gas sensor material associated with its properties such as good chemical stability at high temperature, high electron mobility and the ability to detect both reductive and oxidative gases [11]. ZnO thin films have been produced as a gas sensing material with different methods such as wet chemical bath deposition (CBD) [12], template-assisted growth [13], metal–organic chemical vapor deposition (MOCVD) [14], chemical vapor deposition (CVD) [15], hydrothermal method [16], electrospinning [17] and many others. Among them, the CBD method is economical, simple and large scale covered [18] compared to other methods which request the presence of some specific satisfactory conditions in holding the experiment and thus are more complex. CBD is very interesting because of its easy production with the use of aqueous solvents, non-toxic waste compared to organic compounds and relatively controlled growth. One characteristic in the chemistry of zinc is the tendency of zinc hydroxide to easily undergo dehydration reactions forming the oxide phase, which allows to obtain high ZnO crystal quality even for low-temperature processing [18].

Many researchers have tried to control the sensing performance of the ZnO using different production methods, surface engineering and the utilization of dopant materials. Varudkar et al. have synthesized Al-doped ZnO nanoparticles as gas sensors for the detection of ammonia [19]. Karthik et al. have deposited pure and Ni-doped ZnO thin films by dip coating method for propane and CO sensing applications [20]. Radhi Devi et al. have produced Mg-doped ZnO thin films with SILAR method and studied the ammonia vapor sensing applications [21]. Karaduman Er et al. have studied Cd-doped ZnO thin films with different Cd concentrations used as NO gas sensor [22]. Basyooni et al. have reported a sensitivity of 81.9% for 50 sccm CO_2 gas at room temperature using ZnO [23] and 2.5% for 50 sccm CO_2 gas at room temperature using VO_2 [24]. However, the response and response times were quite long (about 300 s, i.e., 5 min). In addition, Mardare et al. have studied Cr-doped TiO_2 structures and examined CO_2 gas detection properties for different Cr doping content. They achieved 9% sensitivity for 10 ppm CO_2 gas at 55 ℃ operating temperature by the 3% Cr-doped TiO_2 structure [25]. Therefore, in this paper, we investigated the peculiar characteristics of the Cd-doped ZnO thin films produced by CBD method with the aim to analyze the sensing properties of CO_2 gas. The main goal of this study is to produce sensor materials that operate at low temperature and have high sensitivity as well as short response and recovery times. For this aim, various characterizations were carried out to investigate the structural, morphological, optical and gas sensing properties of

the synthesized Cd-doped ZnO thin films. Compared with previously reported results in literature, the fabricated gas sensors seem to be promising in the detection of CO_2 gas at relatively acceptable temperatures and concentrations with high sensitivity as well as short response and recovery times.

2 Experimental setup

All chemicals were of analytical grade and used without any further purification. Zinc acetate dihydrate $(Zn(CH_3CO_2)_2.2H_2O)$ (99%), cadmium acetate dihydrate $(C_4H_6CdO_4)$ (99%) and ammonium hydroxide solution $(NH_4OH, 28–30\%)$ were used as a zinc source, cadmium source and complex agent, respectively. Glass substrates were cleaned in ultrasonic bath and dried at 80 ℃. 0.1 M of zinc source was dissolved in 100 ml. distilled water. Different amounts of cadmium source were added to the solution and Cd molar ratio in the ZnO solution was kept as 1%, 3%, 5% and 7%. The prepared solutions were mixed onto magnetic stirrer to obtain homogeneous aqueous solution. Drop by drop ammonia was added into solution until pH = 10. All chemicals were mixed on the magnetic stirrer at 80 ± 5 °C after which the substrates were dipped in the prepared hot solution for 20 min. After one day waiting, all synthesized films were annealed at 550 °C for 2 h in the furnace to reduce surface impurities.

The crystallographic structure of the synthesized films was characterized by X-ray diffraction (XRD, Rigaku Ultima-IV X-ray diffractometer) using Cu-Kα radiation source with λ = 1.5405 Å in 25° to 80° 2θ range. The surface morphology of the films was observed through scanning electron microscopy (SEM, JEOL JSM-7100 FESEM) which worked at 8×10^{-1} mbar/Pa vacuum operator and 10 mA current with applied Au–Pd (20–80%) coating on the samples. Raman measurements were done by Raman spectrometer (JASCO NRS4500 Confocal Microscope) with wavelength range: 100 to 8000 cm^{-1}, maximum resolution: 2 cm^{-1}, laser: 532 nm, 785 nm. To study the optical properties of the thin films, transmittance measurements were carried out using ultraviolet–visible (Perkin-Elmer UV–Vis Lambda 2S Spectrometer) with a 300-nm filter wavelength. All characterization measurements were done at room temperature.

The gas sensing properties were analyzed in a home-made computer-controlled measurement system, which was described in detail in our previous studies [26, 27]. Mass flow controllers (MKS series) to control the gas concentration, LakeShore 325 temperature controller to change the temperature of the test chamber, Keithley 2400 source meter to carry out the current–voltage (IV) measurement and Honeywell HIH-4000 humidity sensors to keep the humidity constant at about 25% were used in the test system. In
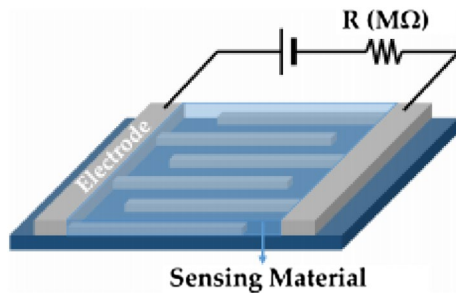
Fig. 1 A schematic diagram of sensing film measuring setup

addition, a computer collected all the data in real time with corresponding data operating hardware and software. A schematic diagram of the sensing film measuring setup is given in Fig. 1.

3 Results and discussions

3.1 XRD analysis

Figure 2 depicts the XRD patterns of pure and Cd-doped ZnO thin films. The peaks are associated with JCPDS card No.36–1451 and show the hexagonal wurtzite structure of ZnO [28]. CdOH started to appear in the crystal structure at and above 3% Cd doping at a diffraction angle 33.9º. It is thought to arise from the utilized production method. It was observed that the peak intensity increased as the Cd contribution ratio increased.

Detailed structural parameters, like lattice constants 'a' and 'c,' aspect ratio, bond length, average crystallite size, dislocation density, strain, atomic packing fraction (APF), volume of nanoparticles and volume of unit cell, are listed in Table 1.

The values of lattice constants 'a' and 'c' were calculated by Eq. (1) [29];

$$\frac{1}{d^2} = \frac{4}{3}\left(\frac{h^2 + hk + l^2}{a^2}\right) + \frac{l^2}{c^2} \tag{1}$$

where h, k and l indicate the miller indices, a and c are the lattice parameters, and d is the inter-planar spacing. The calculated lattice constants are given in Table 1. All parameters are consistent with previously reported results in the literature [30, 31]. The average crystallite sizes of the films were estimated from X-ray line broadening of the preferential orientation peaks using Debye Scherrer's formula [32];
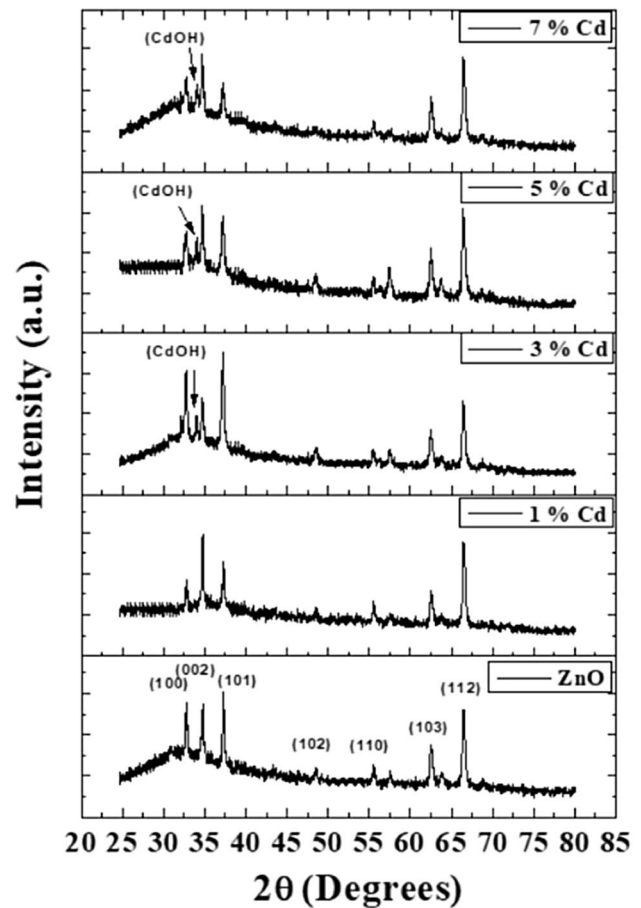
$$D = \frac{0.94\lambda}{\beta \cos\theta} \tag{2}$$

Fig. 2 XRD patterns of pure and Cd-doped ZnO thin films

where λ is the wavelength of X-ray radiation, β is the full width at half maximum (FWHM), and θ is the diffraction angle. Ravichandran et al. have reported that the crystallite size of the ZnO:Cd:F has no linear change depending on the doping concentration of Cd and F. While an increase was observed in 5% and 10% Cd doping concentrations, a decrease was observed in 15% and 20% Cd concentrations [33]. However, Rana et al. have showed that the crystallite size of cadmium-doped zinc oxide samples has a linear decrease with increasing doping concentration [34]. In this study, a decrease in crystallite size was observed up to 3% Cd doping followed by an increase with the further increase in doping content. The change of the crystallite size associated with doping concentration may be explained based on the fact that Cd dopants exert drag forces on the boundary motion and grain growth. And also, increasing the doping concentrations raises the number of point defects and results in a higher grain boundary mobility and grain growth rates [35]. Lattice strain formula is given by Eq. (3) [36];

Table 1 XRD parameters of pure and Cd-doped ZnO thin films

	Lattice parameters		Aspect ratio 'c/a'	Bond length 'L'(Å)	Crystallite size 'D'(nm) From XRD	Dislocation density 'δ' (X10⁻⁴)	Strain 'ε'	APF	Volume of the nanoparticle	Volume of unit cell 'V' (Å)³	No. of unit cells
	'a=b'(Å)	c'(Å)									
ZnO	3.1512	5.1810	1.6441	1.94	67	2.22	0.0569	0.74	157,477	44.5	3538
1% Cd-doped	3.1512	5.1504	1.6550	1.9386	63	2.51	0.0607	0.74	130,920	44.2	2961
3% Cd-doped	3.1512	5.1702	1.6407	1.9395	40	6.25	0.097	0.74	33,510	44.4	754
5% Cd-doped	3.1512	5.1810	1.6441	1.94	53	3.55	0.0723	0.74	77,951	44.5	1751
7% Cd-doped	3.1512	5.1810	1.6441	1.94	55	3.30	0.0699	0.74	87,113	44.5	1957

$$\varepsilon = \frac{\beta \cos\theta}{4} \tag{3}$$

The highest lattice strain was exhibited by the 3% Cd-doped ZnO film. A value associated with strain, dislocation density is calculated by Eq. (4) [37];

$$d = \frac{1}{D^2} \tag{4}$$

The dislocation density is a measure of the number of dislocations in a unit volume of a crystalline material. 3% Cd-doped ZnO has the highest dislocation density compared to other sensors. Equation (5) was used to calculate the volume of the unit cell (ϑ) for hexagonal system [36];

$$\vartheta = \frac{\sqrt{3}}{2}a^2 c \tag{5}$$

Bond length (L) was calculated by the relation given in Eq. (6) [38];

$$L = \sqrt{\left(\frac{a^2}{3} + \left(\frac{1}{2} - u\right)^2 c^2\right)} \tag{6}$$

where a and c are lattice parameters, and u is defined as positional parameter of the wurtzite structure which is calculated by Eq. (7) [36];

$$u = \frac{a^2}{3c^2} + 0.25 \tag{7}$$

'u' parameter is 0.37 and bond length is 1.94 nm for all the films. These values are consistent with bulk zinc (1.97 nm). Atomic packing fraction (APF) was determined by Eq. (8) [39];

$$APF = \frac{2\pi a}{3\sqrt{3}c} \tag{8}$$

The volume of the particles (V) was calculated using Eq. (9), and the volume of hexagonal unit cell has been estimated from ϑ. Then, the ratio (V/ ϑ) gives the number of unit cell present in a grain [36];

$$V = \left(\frac{4}{3}\right)\pi\left(\frac{D}{2}\right)^3 \tag{9}$$

3.2 SEM analysis

Figure 3 depicts the SEM images of pure and Cd-doped ZnO thin films. It shows a large variety of nanostructures randomly distributed over the film surface depending on the Cd doping. Figure 3a shows the pure ZnO which has a smooth and homogeneous structure. Figure 3b depicts the 1% Cd-doped ZnO film. It has a wire-like and chamber-style
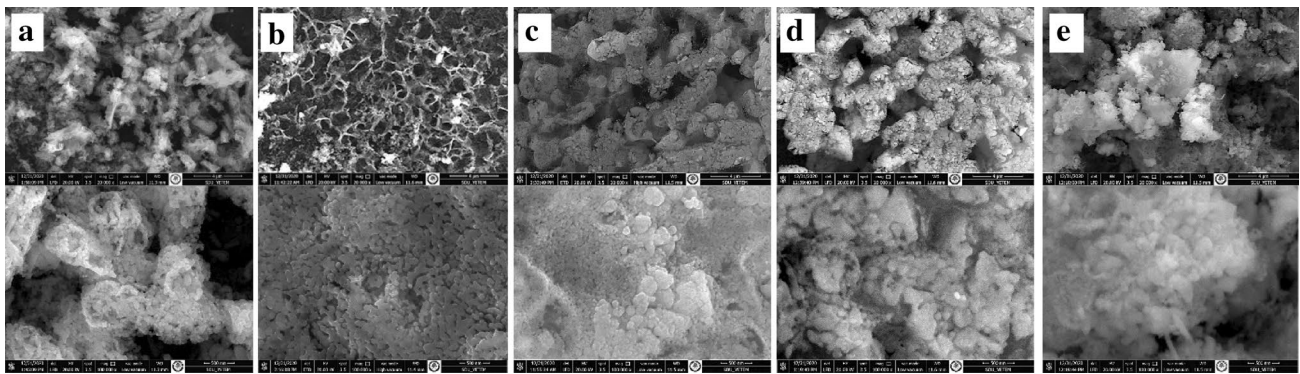
Fig. 3 SEM images of **a** pure, **b** 1% Cd-doped, **c** 3% Cd-doped, **d** 5% Cd-doped and **e** 7% Cd-doped ZnO thin films with (top) 20,000 and (bottom) 100,000 magnifications

surface structure. The types of nanostructures have potential use as gas sensors, dye-synthesized solar cells, energy storage device, etc. The 1% Cd-doped ZnO film exhibited a quite different structure. The variation of morphology with Cd content can be mainly attributed to the solubility of Cd precursor in ZnO aqueous solution [40]. Similar agglomerative composite formations and change in morphology with Cd content were reported in the literature by Kurajica et al. [41]. It was observed that structures with larger grains were formed in 3% (Fig. 3c), 5% (Fig. 3d) and 7% (Fig. 3e) Cd-doped ZnO films. This can be associated with the synthesis method and details of the production technique. Different nanostructures can be seen in Cd-doped thin films produced by different synthesis techniques.

3.3 UV–Vis analysis

Figure 4 depicts the transmittance spectra of pure and Cd-doped ZnO thin films. Obviously, in the visible region, the films are transparent and their transmittance varies roughly between 68 and 75%. The ultraviolet absorption edge corresponding to pure ZnO film undergoes a redshift with the increase in cadmium content, or in other words, the transmittance decreased with increase in Cd concentrations [43]. The direct bandgap values were calculated using Tauc plot [42] as 3.27 eV, 3.25 eV, 3.24 eV, 3.22 eV and 3.16 eV for pure ZnO, 1% Cd-doped, 3% Cd-doped, 5% Cd-doped and 7% Cd-doped ZnO films, respectively. As Cd doping content increased the bandgap values decreased. This decrease can be related to the fact that the bandgap of CdO (bulk value 2.23 eV) is less than that of ZnO (bulk value 3.32 eV) [44, 45]. Despite the expected increase in free charge carrier concentration with Cd doping and the awaited blue shift in transmittance spectra, a prominent red shift was observed. This can be linked to the fact that free carrier absorption in semiconductors can be hard to occur in high-energy bands,
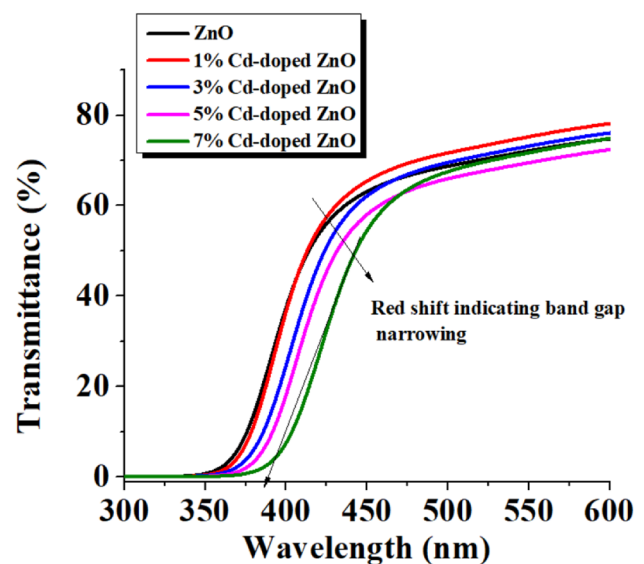

Fig. 4 Transmittance spectra of pure and Cd-doped ZnO thin films at room temperatures

and hence, the red shift indicates that the bandgap itself must have been significantly modulated [43].

The first derivative of the optical transmittance is calculated for estimating the absorption band edge of the films. The curves of $dT/d\lambda$ versus wavelength were plotted, as shown in Fig. 5. As seen in Fig. 5, the peaks, which correspond to the absorption band edge, shifted toward longer wavelengths with the increase in Cd doping content. Similar results have been reported earlier in the literature by [46] and [47].

Refractive indexes of all films were calculated by five different methods (Eqs. (10)-(14)) using bandgap energies. Naccarato et al. have shown that if $n > 2$ and $Eg > 3$, the transition is classified as transition metals (TMs) with empty d shell (e.g., V^{5+}) [48]. The estimated refractive
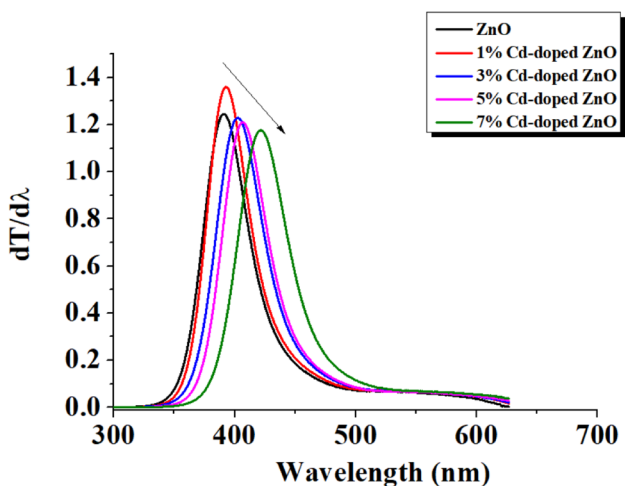
Fig. 5 dT/dλ versus wavelength plots of pure and Cd-doped ZnO thin films

indices are graphed in Fig. 6. As shown in Fig. 6, the refractive index depends on the Cd concentration.

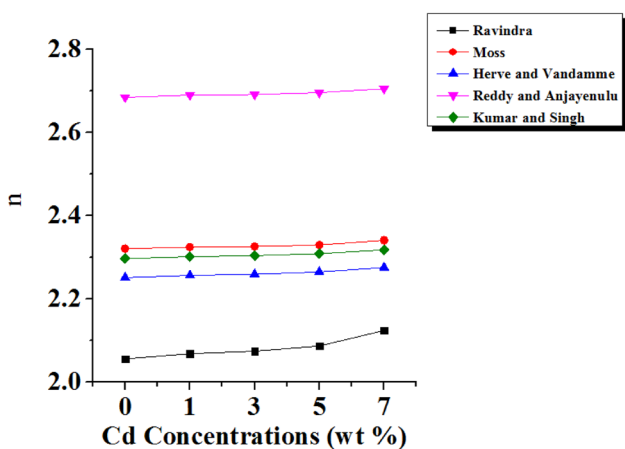|		
$n = 4.084 - 0.62E_g$	Ravindra et al. [49]	(10)
$n = \left(\frac{95}{E_g}\right)^{1/4}$	Moss et al. [50]	(11)
$n = \sqrt{1 + \left(\frac{13.6}{E_g + 3.47}\right)^2}$	Hervé and Vandamme et al. [51]	(12)
$n = \left(\frac{154}{E_g - 0.305}\right)^{1/4}$	Reddy and Anjayenulu et al. [52]	(13)
$n = 3.3668(E_g)^{-0.32234}$	Kumar and Singh et al. [53]	(14)

Fig. 6 Plots of refractive index versus Cd concentration of all synthesized films based on five different models

3.4 Raman analysis

Raman spectra of pure and Cd-doped ZnO thin films are given in Fig. 7. As this technique is more sensitive than XRD to the molecular environment, we can observe the degree of crystallinity, structural disorder and the microstructural and nanostructural defects present in the material [54]. Dominant peaks at around 101 and 439 cm^{-1} are the characteristic peaks of the wurtzite structure of ZnO. They are assigned to the low- and high-E_2 modes [55]. In the present study, the E_2 vibration mode at 435 cm^{-1} is characteristic of the wurtzite phase and its value is slightly lower around 439 cm^{-1} for the stress free bulk ZnO [55]. We observe an additional band at 280 cm^{-1} in the 1% Cd-doped ZnO. This mode corresponds to the silent mode of wurtzite-ZnO which originates from the breakdown of the translational crystal symmetry induced by defects and impurities [56]. These bands to intrinsic host-lattice defects related to the doping because most of the bands observed under Cd doping were also observed in other doped samples [54]. The results indicate that the Cd-doped ZnO thin films could still retain their wurtzite structure; the A_1 (LO) mode at 574 cm^{-1} resulting from oxygen vacancies and zinc interstitials was observed to be very strong in the Raman spectra. In our study, the shifting from 584 to 571 cm^{-1} was seen through the increase in Cd concentration from 0 to 7%. This may be due to bigger isoelectronic
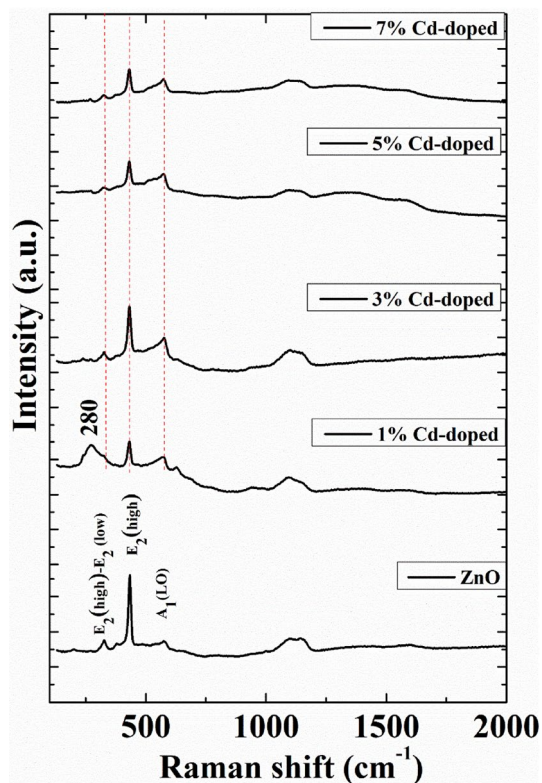

Fig. 7 Raman spectra of pure and Cd-doped ZnO thin films

Cd (0.23 Å) substitution at Zn atom that expands lattice. The spectra show several peaks characteristic of vibrational modes of ZnO and CdO [57]. Therefore, it can be concluded that with the increase in the doping ratio, the concentration of the bridging oxygen vacancies gradually increases, which helps in improving the gas sensing performance [58].

3.5 Gas sensing analysis

Based on literature studies, it can be said that the change of sensor response does not only depend on the gas in the environment but also on the operating temperature of the sensor material. So, choosing an optimal operating temperature is a major factor for keeping the stability of a sensor. The switching of the gas response with different operating temperatures in the presence of 100 ppm CO_2 gas is shown in Fig. 8. The responses to 100 ppm of CO_2 gas at room temperature (inset of Fig. 8) were calculated as 0.12%, 3.29%, 8.36%, 3% and 2.5% for pure, 1% Cd-doped, 3% Cd-doped, 5% Cd-doped and 7% Cd-doped ZnO sensors, respectively. A gradual increase was observed in the response as the temperature increased up to 125 °C, followed by a gradual decrease after 125 °C for all Cd-doped ZnO sensors. However, for pure ZnO, the response continued to increase as the temperature increased. Since the responses of other samples started to decrease, the experimental measurements were terminated at a temperature of 250 °C. Clearly, the operating temperature of the synthesized sensors is 125 °C in the investigated temperature range. The responses to 100 ppm of CO_2 gas at 125 °C were calculated as 2.78%, 61.4%, 88.24%, 31% and 25.6% for pure, 1% Cd-doped, 3% Cd-doped, 5% Cd-doped and 7% Cd-doped ZnO sensors, respectively. Maximum response was seen at the optimal operating temperature and decreased after that temperature. Such behavior is known as the 'volcano curve.' It says that a reduction of the absorbing
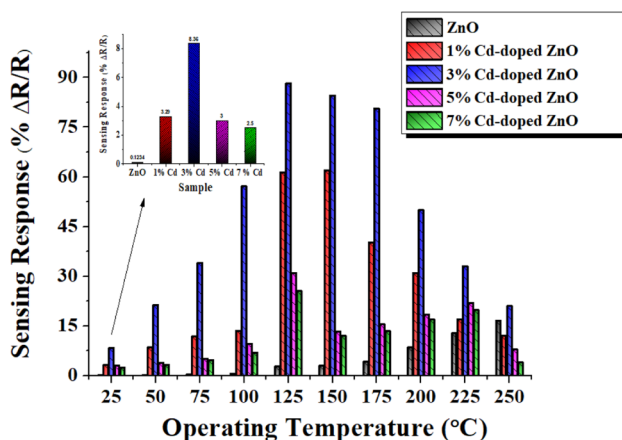
oxygen molecules can be seen upon increasing the temperature above some ideal point (optimum point). The energy of oxygen atoms sent to the surface is increased with the increase in temperature which causes instability and prevents the desired reaction with the target gas. For this reason, each of the sensor materials has a specific operating temperature.

Obviously from Fig. 8, the highest response was obtained by the 3% Cd-doped sensor irrespective of temperature. A possible explanation of this result based on the corresponding structural parameters can be made as follows: small crystallite size increases the surface to volume ratio and hence provides more active sites for the adsorption of O_2 and analyte gases [59]. Indeed, from the XRD analysis, 3% Cd-doped ZnO films showed the smallest crystallite size among all others. Sholehah et al. [60] proved the same relation in their study. In addition to that, 3% Cd-doped ZnO films recorded the highest dislocation density which is associated with lattice imperfection and can have considerable effect on gas sensing properties. Zhou et al. [61] and Choi et al. [62] showed that lattice imperfections can be considered as oxygen deficiencies which can act as important reaction sites.

After determining the operating temperature, dynamic measurements were started for different gas concentrations at a constant temperature of 125 °C. Examinations of the effect of gas concentrations under constant temperature on the responses of the samples to these gas concentrations were carried out. Figure 9 shows the dynamic gas sensing measurements for all sensors. It can be seen from the measurements that the films showed a different response intensity for each gas concentration and returned to the initial value when air was sent to the test cell. Therefore, the synthesized thin films can be used as sensor materials in commercial applications. The responses to 10 ppm CO_2 gas were calculated as 5.29%, 6.36%, 2% and 1.21% for 1% Cd-doped, 3% Cd-doped, 5% Cd-doped and 7% Cd-doped ZnO sensors, respectively.

The responses increased with increase in gas concentrations and a linear relationship was found, as seen in Fig. 10. The increase in responses with the increase in gas concentration indicates that the sensing material responds differently to each gas concentration, a kind of evidence of 'selectivity against different ppm concentrations.' Obtaining approximately the same responses against different gas concentrations is undesirable in gas sensor applications, especially in matters where human health and life quality are concerned. Gancarz et al. [63] and Liu et al. [64] have reported that linearity is an important factor for electronic nose applications. Especially, Liu et al. have studied lung cancer detection via breath analysis, and so in such critical situations, selectivity and classification performance become the main target of their study on electronic nose [64].

The relationship between response (S) and target gas concentration (C) can be empirically described by $S = a \times C^b$,
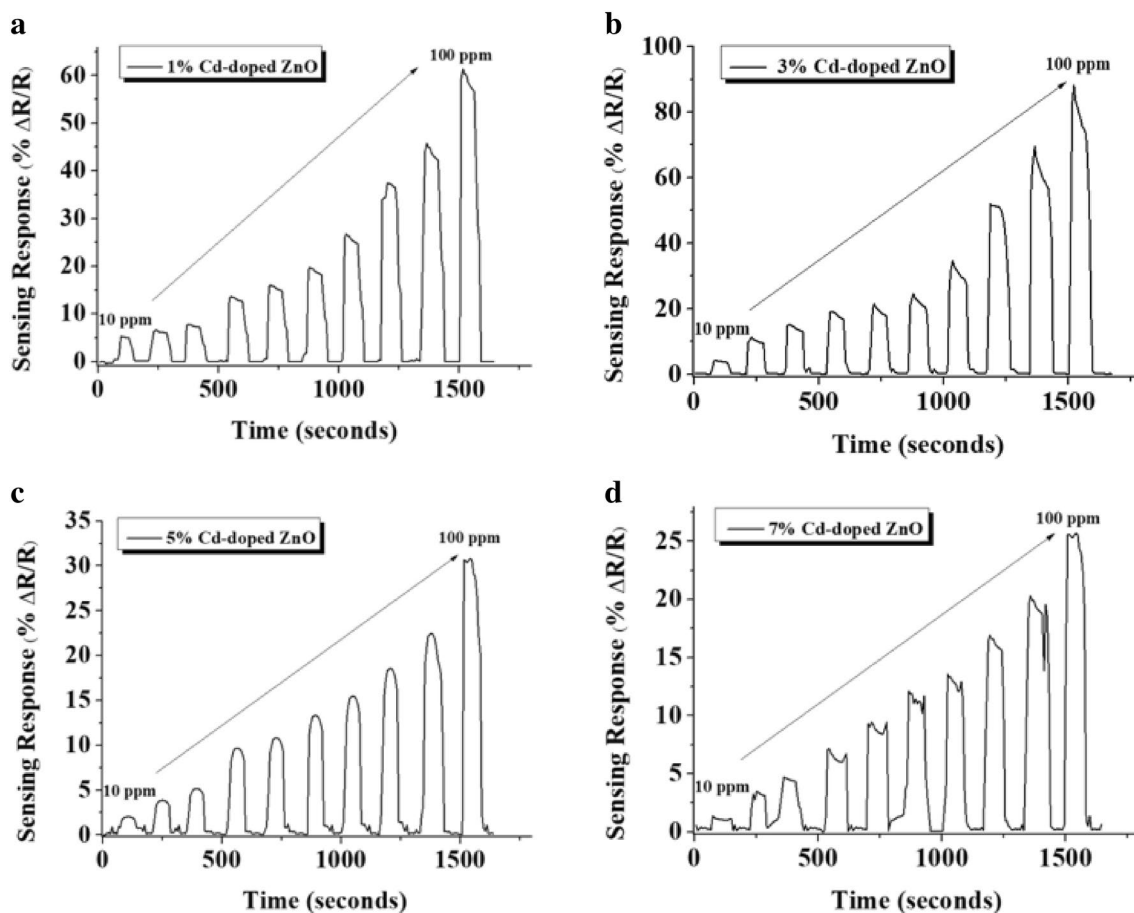

Fig. 8 CO_2 response of fabricated sensors depending on the operating temperatures

Fig. 9 The dynamic gas sensing measurements for (a) 1% Cd-doped, (b) 3% Cd-doped, (c) 5% Cd-doped and (d) 7% Cd-doped ZnO sensors at 125 °C
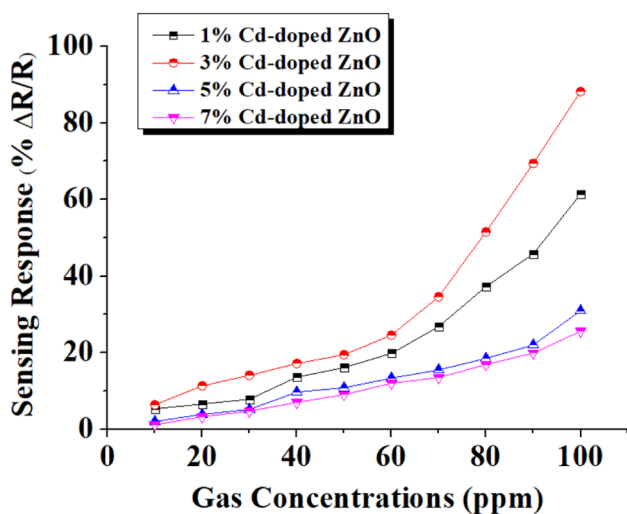

Fig. 10 The sensing responses versus gas concentrations for Cd-doped ZnO sensors

where a and b are constants [65]. At a certain operating temperature, the previous equation can be rewritten as $\log(S-1) = b \times \log(C) + \log(a)$. As shown in Fig. 11, a good linear relationships existed between the logarithm of the responses S and the logarithm of the concentrations in the studied concentration ranges, which is consistent with the power law theory of semiconductor sensors. Indeed, all films showed a linear relationship with the CO_2 gas concentrations in logarithmic forms in two separate regions (region I: 10 ppm–30 ppm and region II: 40 ppm–100 ppm). Correlation coefficients of the Cd-doped ZnO sensors found from Fig. 11 are given in Table 2. From Table 2, 0.9947/0.9928 was calculated as the correlation coefficient value for 3% Cd-doped ZnO sensor. As a result of this, we could say that this sample has a good potential for detecting CO_2 gas.

As important parameters in optimizing any gas sensor performance for practical applications, response and recovery times explained, respectively, as the time required to reach 90% of the final equilibrium value and the time required to return back to 90% of the initial equilibrium value [66] of Cd-doped ZnO sensors for different gas
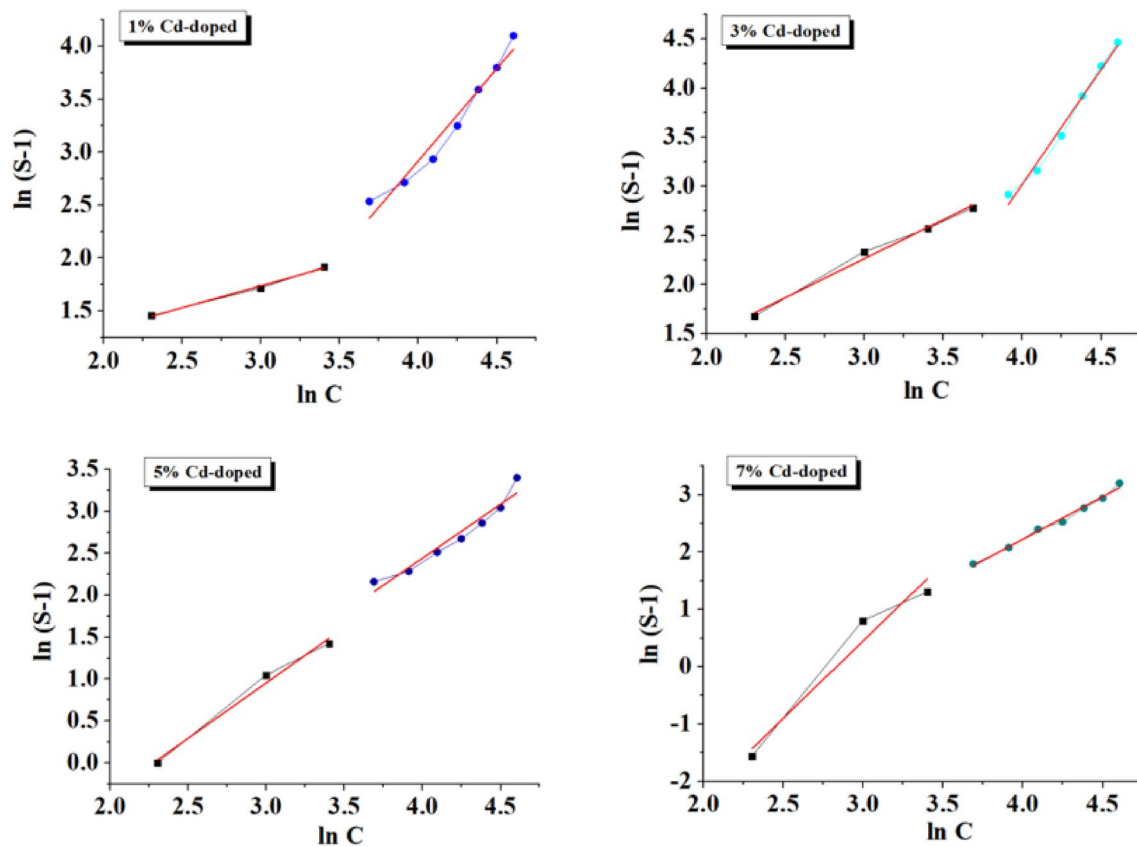
Fig. 11 ln (S-1) versus ln C for all Cd-doped ZnO sensors

Table 2 The gas sensing parameter of all Cd-doped ZnO sensors

Parameters	1% Cd-doped	3% Cd-doped	5% Cd-doped	7% Cd-doped
Linearity range, ppm	10–30/ 40–100	10–40/50–100	10–30/40–100	10–30/40–100
Slope	0.4147/1.7446	0.7925/2.3392	1.3205/1.2872	2.6972/1.4876
Correlation coefficient	0.9973/0.9811	0.9947/0.9928	0.9934/0.9705	0.9785/0.9949
R^2	0.9826/0.9551	0.9843/0.9821	0.9738/0.9303	0.9151/0.9879

concentrations were measured at 125 °C (Fig. 12). The fastest response and recovery times were recorded by 3% Cd-doped ZnO sensor, where the response/recovery times were calculated as 19 s/1 s for 10 ppm CO_2 gas and 11 s/10 s for 100 ppm CO_2 gas.

Selectivity measurements were carried out at the operating temperature of 125 °C as shown in Fig. 13. Benzene, hydrogen, ammonia, methanol, CO_2, acetone and CO gases were used as target gases. It can be seen that 3% Cd-doped ZnO sensor exhibited the best selective properties compared to other sensors for CO_2 gas. It can be said that CO_2 gas molecules are accelerated with the charge transfer from the sensor surface. Electronegativity is defined when an atom itself gets attracted toward the shared electron pair. The electronegativity of oxygen (3.44) is greater than that of carbon atoms (2.55). So the shared electrons between two dissimilar

atoms are lightly pulled toward the oxygen atoms. As the negative charge (δ^-) is established on the oxygen atoms, this causes a positive charge (δ^+) on the carbon atom of CO_2, and the bond becomes polar and consists of 2 symmetric dipoles where negative and positive pole centers become overlaid [67]. Both oxygen atoms are connected to the carbon atom with two double bond ($O^- = C^+ = O^-$). Known as an oxidizing agent, in other words CO_2 is able to take electrons from the metal oxide film surfaces increasing the number of holes and therefore the film resistance [24, 68].

The best gas sensing results were adopted by the 3% Cd-doped ZnO sensor, and so the next measurements were done on this sensor. First, we carried out the long-term stability measurements. In practical applications, the long-term stability of the sensor is also an important parameter [69]. The credibility of the sensor and its duration of service can be
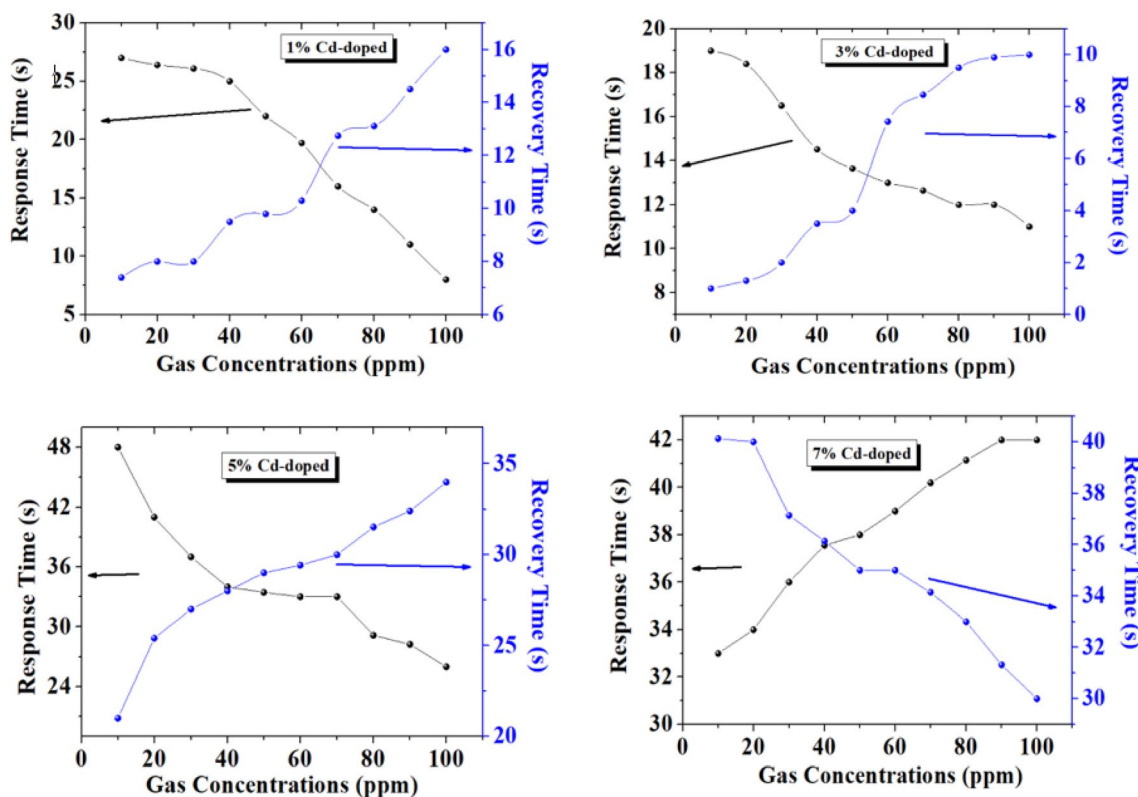
Fig. 12 Response and recovery times of Cd-doped ZnO sensors for different gas concentrations at 125 °C

approved by the long-term stability. In 30 days, the response to 100 ppm CO_2 gas of the sensor was tested at the optimum operating temperature of 125 °C, as shown in Fig. 14a. The response dropped from 88.25% to 88.20% during the first 7–8 days and then remained stable at the same value

Fig. 13 Selectivity measurements of Cd-doped ZnO sensors at the operating temperature of 125 °C

(about 88.20%). Obviously, the response exhibited a stable behavior for about 22 days in the investigated duration range. This result indicates that the sensing material has acceptable performance in long-term stability. Figure 14b shows the repeatability of 3% Cd-doped ZnO sensor. It exhibited approximately the same response over 10 cycles.
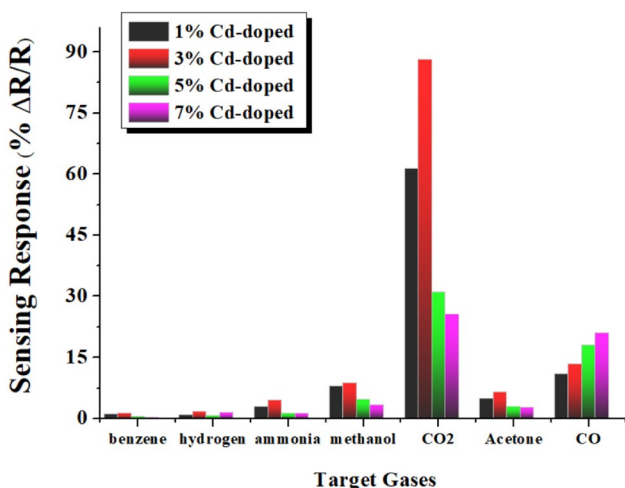
Generally, semiconducting metal oxides gas sensing mechanism is based on changes in the electrical resistance while in contact with input gas (oxidizing/reducing) [70]. Two main reactions can take place on the gas sensing surface. The first reaction occurs when the sensor surface chemically adsorbs the oxygen in the air as O_2^- (molecular), O^- (atomic) and OH^- (hydroxyl). Electrons in the conduction band transfer toward the adsorbed oxygen. As a result of this transfer, oxygen atoms cling to the surface and a space charge region forms. The second reaction takes place between the target gas molecules and the adsorbed oxygen atoms [70]. CO_2 molecules react with O^- ions. With the help of O^- ions, CO_2 molecules capture the electrons from the surface and reduce the electron concentration. The decrease in the electron concentration leads to an increase in resistance. The increase in resistance is also caused by the increase in barrier height that leads to a decrease in the electron flow.
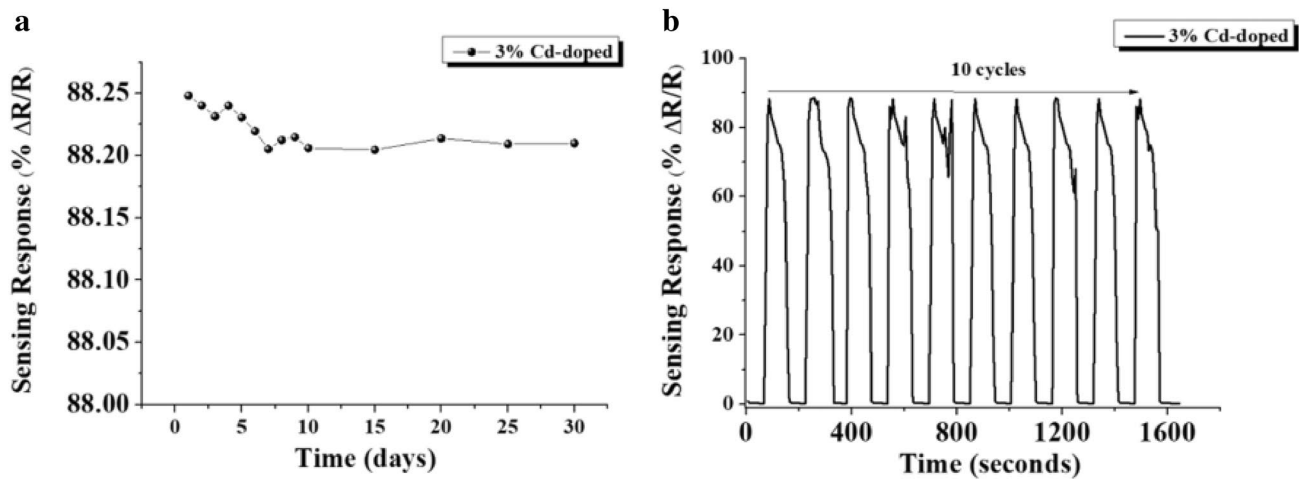
a

b

Fig. 14 a The stability at inter-day and (b) the repeatability at intra-day of 3% Cd-doped ZnO sensor at 125 °C for 100 ppm CO_2 gas

Table 3 A literature review on CO_2 gas sensors

Material	Types of sensor	Working temp (℃)	Sensing response	CO_2 Concentrations	Author
Calcium-doped ZnO	Chemiresistor	350	55.00%	50 ppm	[71]
ZnO	Chemiresistor	350	64%	400 ppm	[72]
La_2O_3	Chemiresistor	250	64%	400 ppm	[73]
In_2Te_3	Chemiresistor	RT	50%	1000 ppm	[74]
CN_x/p-Si	Chemiresistor	RT	1.90	8 mbar	[75]
ZnO thin films	Chemiresistor	100	2.17	8.5 mbar	[76]
ZnO nanowires	Chemiresistor	150	3.7	15 1/min	[77]
In-doped ZnO	Chemiresistor	200	16	–	[78]
Cd-doped ZnO	Chemiresistor	125	88	100 ppm	This work

Taking target gas concentration and operating temperature factors into consideration, the responses obtained by the fabricated sensors are acceptable responses in the process of CO_2 gas detection compared with previous literature studies summarized in Table 3. A careful examination of Table 3 can tell that the fabricated sensors of this study have the ability to detect CO_2 gas at relatively low concentrations (100 ppm) compared to other reported studies at room temperature. Thus, our sensors seem to be promising for commercial CO_2 gas sensor applications.

4 Conclusions

In summary, pure and Cd-doped (with 1%, 3%, 5% and 7% Cd content) ZnO thin films were produced by chemical bath deposition method and used as gas sensors to optimize the detection of the hazardous CO_2 gas. From the CO_2 gas sensing analysis, all sensors recorded a maximum response at a temperature of 125 °C which was regarded as the operating temperature of the sensors. The responses to 100 ppm at 125 °C were calculated as 2.78%, 61.4%, 88.24%, 31% and 25.6% for pure, 1% Cd-doped, 3% Cd-doped, 5% Cd-doped and 7% Cd-doped ZnO sensors, respectively. 3% Cd-doped ZnO sensor exhibited the best CO_2 gas sensing properties in terms of short response/recovery times (19 s / 1 s for 10 ppm CO_2 gas), good selectivity as well as high stability and reproducibility.

Declarations

Conflict of interest The authors declare that they have no known competing financial interests or personal relationships that could have appeared to influence the work reported in this paper.

References

1. G.A. Florides, P. Christodoulides, Environ. Int. **35**, 390–401 (2009)
2. M. Amarnath, K. Gurunathan, J. Alloys Compd. **857**, 157584 (2021)
3. C. Le Quéré, G.P. Peters, P. Friedlingstein, R.M. Andrew, J.G. Canadell, S.J. Davis, R.B. Jackson, M.W. Jone, Nat. Clim. Chang. **11**, 197–199 (2021)
4. S. Neethirajan, M.S. Freund, D.S. Jayas, C. Shafai, D.J. Thomson, N.D.G. , White Biosyst. Eng. **106**, 395–404 (2010)
5. N. Barsan, D. Koziej, U. Weimar, Sens. Actuators B **121**, 18–35 (2007)
6. G. Lei, C. Lou, X. Liu, J. Xie, Z. Li, W. Zheng, J. Zhang, Sens. Actuators B **341**, 129996q (2021)
7. B. Salah, A.I. Ayesh, Mater. Chem. Phys **266**, 124597 (2021)
8. M. Sun, S. Zhang, Z. Zhang, H. Zhang, Y. Wang, X. Jing, X. Song, J Mater Sci **56**, 11801–11813 (2021)
9. Z. Zhang, M haq, Z Wen, Z Ye, L Liping Zhu, , Appl. Surf. Sci. **434**, 891–897 (2018)
10. D Yang, RA Gopal, Y Lee, S Kim, H Jeon, V E Sathishkumar, A M Al-Mohaimeed, W A Al-onazi, T saad Algarni, D Choi, (2021) J. King. Saud. Univ. Sci. 33(3): 101397
11. M.K. Roul, S.K. Pradhan, K.D. Song, M.J. Bahoura, J Mater Sci **54**, 7062–7071 (2019)
12. F. Sarf, I Karaduman Er, E. Yakar, S. Acar, J. Mater. Sci.: Mater. Electron. **31**, 10084–10095 (2020)
13. M. Habib, S.S. Hussain, S. Riaz, S. Naseem, Mater. Today: Proceed. **2**, 5714–5719 (2015)
14. S. Pati, P. Banerji, S.B. Majumder, Sens. Actuators A **213**, 52–58 (2014)
15. S. Vallejos, F. Di Maggio, T. Shujah, C. Blackman, Chemosensors **4**, 4 (2016)
16. IKaraduman Er, İA Yıldız, T Bayraktar, S Acar, A Ates, (2021) J. Mater. Sci: Mater. Electron. 32: 8122-8135
17. P.V. Morais, P.H. Suman, R.A. Silva, M.O. Orlandi, J. Alloys Compd. **864**, 158745 (2021)
18. M.F. Nurfazliana, M.Z. Sahdan, H. Saim, AIP Conf. Proceed. **1788**, 030091 (2017)
19. H.A. Varudkar, G. Umadevi, P. Nagaraju, J.S. Dargad, V.D. Mote, J Mater Sci: Mater Electron **31**, 12579–12585 (2020)
20. TVKKarthik, M Luz Olvera De La, A Maldonado, RR Biswal, H Gómez-Pozos, (2020) Sensors 20: 6879
21. KRadhi Devi, G Selvan, M Karunakaran, K Kasirajan, L Bruno Chandrasekar, Mohd Shkir, S AlFaify, (2020) J. Mater. Sci: Mater. Electron. 31: 10186-10195
22. I Karaduman Er, (2021) Res. Eng. Struct. Mater https://doi.org/10.17515/resm2020.212ma0901
23. M.A. Basyooni, M. Shaban, M.A. El Sayed, Sci. Reports. **7**, 41716 (2017)
24. S.E. Zaki, M.A. Basyooni, M. Shaban, M. Rabia, Y.R. Eker, G.F. Attia, M. Yılmaz, A.M. Ahmed, Sens. Actuators A **294**, 17–24 (2019)
25. D. Mardare, N. Cornei, C. Mita, D. Florea, A. Stancu, V. Tirona, A. Manole, C. Adomnitei Ceram. Int. **42**, 7353–7359 (2016)
26. I. Karaduman Er, M.A. Yıldırım, H.H. Örkçü, A. Ateş, S. Acar, Appl. Phys. A **127**(4), 230 (2021)
27. F. Ozutok, I. Karaduman, S. Demiri, S. Acar, J. Elec. Mater. **47**, 2648–2657 (2018)
28. IKaraduman Er, T Nurtayeva, M Sbeta, AO Cagirtekin, S Acar, A Yildiz, (2019) J. Mater. Sci: Mater. Electron. 30: 10560-10570
29. F. Zahedi, R.S. Dariani, S.M. Rozati, Bull. Mater. Sci. **37**(3), 433–439 (2014)
30. E. Muchuweni, T.S. Sathiaraj, H. Nyakotyo, Mater. Res. Bull. **95**, 123–128 (2017)
31. S.D. Senol, E. Ozugurlu, L. Arda, Ceram. Inter. **46**(6), 7033–7044 (2020)
32. M. Mujahıd, Bull. Mater. Sci. **38**(4), 995–1001 (2015)
33. K. Ravichandran, K. Saravanakumar, R. Chandramohan, V Nandhakumar Appl. Surf. Sci. **261**, 405–410 (2012)
34. N. Rana, S. Chand, K.A. Gathania, Ceram. Inter. **41**(9), 12032–12037 (2015)
35. AJ Najim, JM Rozaiq, (2013) Int. Lett. Chem, Phys Astr 15: 137-150 https://doi.org/10.18052/www.scipress.com/ILCPA.15.137
36. M. Sathya, K. Pushpanathan, Appl. Surf. Sci. **449**, 346–357 (2018)
37. R. Mariappan, V. Ponnuswamy, A. Chandra Bose, A. Chithambararaj, R. Suresh, M. Ragavendar, Superlattices Microstruct. **65**, 184–94 (2014)
38. G. Srinivasan, R.T. Rajendra Kumar, J. Kumar, (2007) J. Sol-Gel. Sci. Technol. 43: 171
39. Ö. Bilgili, J. Baun Inst. Sci. Technol. **23**(1), 50–64 (2021)
40. S. Kurajica, V. Mandić, G. Matijašić, I.K. Munda, K. Mužina, Sci Eng Compos Mater **26**, 482–490 (2019)
41. J. Zhang, S.-Q. Zhao, K. Zhang, J.-Q. Zhou, Y.-F. Cai, Nanoscale Res Lett **7**, 405 (2012)
42. U. N. Maiti, P. K. Ghosh, Sk. F. Amed, M. K. Mitra, K. K. Chattopadhyay, (2007) J. Sol-Gel Sci Techn. 41: 87–92
43. A.D. Acharya, S. Moghe, R. Panda, S.B. Shrivastava, M. Gangrade, T. Shripathi, D.M. Phase, V. Ganesan, Thin Solid Films **525**, 49–55 (2012)
44. K. Shan, G.X. Liu, W.J. Lee, B.C. Shin, J. Cryst. Growth **291**, 328 (2006). https://doi.org/10.1016/j.jcrysgro.2006.03.036
45. X.D. Zhang, M.L. Guo, W.X. Li, C.L. Liu, J. Appl. Phys. **103**, 063721 (2008). https://doi.org/10.1063/1.2901033
46. F. Yakuphanoglu, S. Ilican, M. Caglar, Y. Caglar, Superlattices Microstruct. **47**(6), 732–743 (2010)
47. K. Ravichandran, A. Manivasaham, J. Mater. Sci: Mater. Electron. **28**, 6335–6344 (2017)
48. F. Naccarato, F. Ricci, J. Suntivich, G. Hautier, L. Wirtz, G.-M. Rignanese, Phys. Rev. Materials **3**, 044602 (2019)
49. E. Asikuzun, A. Donmez, L. Arda, O. Cakiroglu, O. Ozturk, D. Akcan, M. Tosun, S. Ataoglu, C. Terzioglu Ceramic Inter. **41**, 6326 (2015)
50. E. Asikuzun, O. Ozturk, L. Arda, C. Terzioglu, J. Mater. Sci. Mater. Electron. **28**, 14314 (2017)
51. Z.K. Heiba, L. Arda, M.B. Mohamed, M.A. Al-Jalali, N. Dogan J. Supercond Nov. Magn **26**, 3299 (2013)
52. N. Üzar, G. Algün, N. Akçay, D. Akcan, L. Arda, J. Mater. Sci. Mater. Electron. **28**, 11861–70 (2017)
53. P.A. Rodnyi, I.V. Khodyuk, Opt. Spectrosc. **111**, 776–785 (2011)
54. D. A. Guzman-Embus, M. F. Vargas-Charry, C. Vargas-Hern Vandez, (2015) J. Am. Ceram. Soc. 98(5): 1498–1505
55. R.A. Zargar, P.A. Ahmad, M.A. Sheer Gogre, M.M. Hassan, Opt. Quantum Electron. **52**, 401 (2020)
56. B. Rahal, B. Boudine, A.R. Khantoul, M. Sebais, O. Halimi, Optik **127**, 6943–6951 (2016)
57. N. Rana, S. Chand, A.K. Gathania, Ceram. Intern. **41**(9-B), 12032–12037 (2015)
58. W. Bi, W. Xiao, S. Liu, J Mater Sci **56**, 6095–6109 (2021)
59. G. Biasotto, M.G.A. Ranieri, C. Foschini, A.Z. Simões, E. Longo, M.A. Zaghete, Ceram. Int. **40**(9), 14991–14996 (2014)
60. A. Sholehah, K. Karmala, N. Huda, L. Utari, N. L. Wulan Septiani, B. Yuliarto, (2021) Sens. Actuators A 331: 112934
61. X. Zhou, A. Wang, Y. Wang, L. Bian, Z. Yang, Y. Bian, Y. Gong, X. Wu, N. Han, Y. Chen, ACS Sens. **3**, 2385–2393 (2018)
62. P. Gyu Choi, T. Fuchigami, K.-i. Kakimoto, Y. Masuda, (2020) ACS Sens. 5: 1665−1673
63. M. Gancarz, U. Malaga-Toboła, A. Oniszczuk, S. Tabor, T. Oniszczuk, M. Gawrysiak-Witulska, R. Rusinek, Food Bioprod. Process. **127**, 90–98 (2021)

64. B. Liu, H. Yu, X. Zeng, D. Zhang, J. Gong, L. Tian, J. Qian, L. Zhao, S. Zhang, R. Liu, Sens. Actuators: B **339**, 129896 (2021)
65. C. Zhu, K. Huang, F. Yuan, C. Xıe, Mater. Sci.-Pol. **32**(2), 181–187 (2014). https://doi.org/10.2478/s13536-013-0168-7
66. T. Thomas, Y. Kumar, J. Alberto, R. Ramón, V. Agarwal, S. Sepúlveda Guzmán, R. Reshmi, S. Pushpan, S. Lugo Loredo, K.C. San al, (2021) Vacuum. 184: 109983
67. I. Karaduman Er, I. A. Yıldız, T. Bayraktar, S. Acar, A. Ates¸ (2021). J Mater Sci: Mater Electron 32: 8122–8135
68. F. Panto, S.G. Leonardi, E. Fazio, P. Frontera, A. Bonavita, G. Neri, P. Antonucci, F. Neri, S. Santangelo, Nanotechnology **29**, 305501 (2018)
69. R. Zhao, J Phys Chem Solids **112**, 43–49 (2018)
70. M. Amarnath, K. Gurunathan, J. Alloys Compd. **857**, 157584 (2021)
71. A. Ghosh, C. Zhang, H. Zhang, S. Shi, Langmuir **35**, 10267–10275 (2019)
72. Y.M. Hunge, A.A. Yadav, S.B. Kulkarni, V.L. Mathe, Sensor. Actuator. B Chem. **274**, 1–9 (2018)
73. A.A. Yadav, A.C. Lokhande, J.H. Kim, C.D. Lokhande, J. Alloys Compd. **723**, 880–886 (2017)
74. P. Matheswaran, R. Sathyamoorthy, K. Asokan, Sensor. Actuator. B Chem. **177**(8), 13 (2013)
75. N. Zouadi, S. Messaci, S. Sam, D. Bradai, N. Gabouze, Mater. Sci. Semicond. Process. **29**, 367–371 (2015)
76. S. Agarwal, P. Rai, E. Navarrete Gatell, E. Llobet, F. Guelle, M. Kumara, K. Awasth, (2019). Sens. Actuators B Chem. 292: 24–31
77. S Roso, F Guell, PR Martı´nez-alanis, A Urakawa, E Llobet, (2016) Sens. Actuators. B Chem. 230: 109-114 https://doi.org/10.1016/j.snb.2016.02.048
78. M. Habib, S.S. Hussain, S. Riaz, S. Naseem, Mater. Today: Proc. **2**, 5714–5719 (2015)